Base Stacking and Sugar Orientations Contribute to Chiral Recognition of Single-Walled Carbon Nanotubes by Short ssDNAs

Sayantani Chakraborty[1], Enrique Ebarguen[1], Kevin E. Chacon[1], Milena Petković[2], Lela Vuković[1]*

[1]Department of Chemistry and Biochemistry, University of Texas at El Paso, El Paso, Texas, United States
[2]University of Belgrade - Faculty of Physical Chemistry, Studentski trg 12-16, 11158 Belgrade, Serbia
Email: lvukovic@utep.edu

Abstract: Single-walled carbon nanotubes (SWNTs) possess exceptional physical and optical properties that make them promising for biomedical and engineering applications. Chirality-pure and enantiopure SWNTs are of particular interest. While single-stranded DNAs were shown to differentially bind and sort SWNTs, the underlying mechanism is not well understood. In this study, we used molecular dynamics simulations to investigate the binding of single and multiple DNA nucleotides to two (7,5) SWNT enantiomers, E1 and E2. Our simulations reveal that nucleotide bases stack closer to the surface of the E2 than the E1 enantiomer. Surprisingly, chiral single and dinucleotides did not exhibit enantiomer-dependent preferences in angular orientations on the SWNT surface. However, ATT trinucleotides exhibited differences in preferred orientations and arrangements of sugar atoms when bound to SWNT enantiomers. Our results suggest that preferred arrangements of DNA sugar moieties may be an important parameter that contributes to the differential binding of DNAs to SWNT enantiomers.

Single-walled carbon nanotubes (SWNTs) possess unique optical, mechanical, thermal, and electronic properties, which make them attractive candidates for various biomedical, engineering, and nanotechnology applications[1–10]. However, bulk samples of synthesized SWNTs usually contain a mixture of nanotubes of different chiralities and thus different physical properties. SWNT chirality is represented by a pair of integers (*n, m*), where *n* and *m* describe the carbon lattice structure and originate from the vector $c = na_1 + ma_2$, where a_1 and a_2 represent the lattice vectors of the graphene sheet that is rolled up to make a carbon nanotube[11–13]. Except for the cases when $n = m$ or $m = 0$, SWNTs are chiral and exist as two enantiomers which are mirror images of each other, where the left-handed isomer is called *M* and the right-handed one is called *P*.[14] The opto-electronic properties of SWNTs have a direct relation to their chirality because the energies and densities of the electronic states of the SWNTs are affected by their transverse structure[15–18].

To use SWNTs with physical and opto-electronic properties specifically fitting the given application need, it would be useful to pre-sort SWNTs into single-chirality enantiopure samples. Previous studies showed that some ssDNAs can differentially bind and sort SWNTs of specific chiralities. For example, chiral SWNTs were bound to ssDNAs and sorted with the help of aqueous two-phase partitioning and chromatographic methods[19–24]. Other recent approaches successfully combined experiments with machine learning to conduct systematic search for DNA sequences to sort chiral carbon nanotubes[25]. Some DNAs were also shown to differentially bind, with low and high affinity, to two enantiomers of the same chirality[26]. In the latter case, even though the SWNT enantiomers are mirror images of each other, two *M* and *P* enantiomers with the same (*n,m*) index interact differently with chiral single stranded DNA molecules.

Despite several theoretical and computational investigations of SWNT sorting[27–29], the molecular mechanism behind the recognition of different chiralities / enantiomers of SWNTs by ssDNAs is not yet well understood, and there are still no established physical principles which could help in prediction of ssDNA sequences which can sort SWNT species. Here, we examine the molecular recognition of SWNTs

by small DNA molecules using classical molecular dynamics (MD) simulations, focusing on the binding of single, di- and trinucleotide DNAs to two enantiomers of (7,5) SWNT. We identify new structural factors associated with distinct binding of small ssDNAs to SWNT enantiomers.

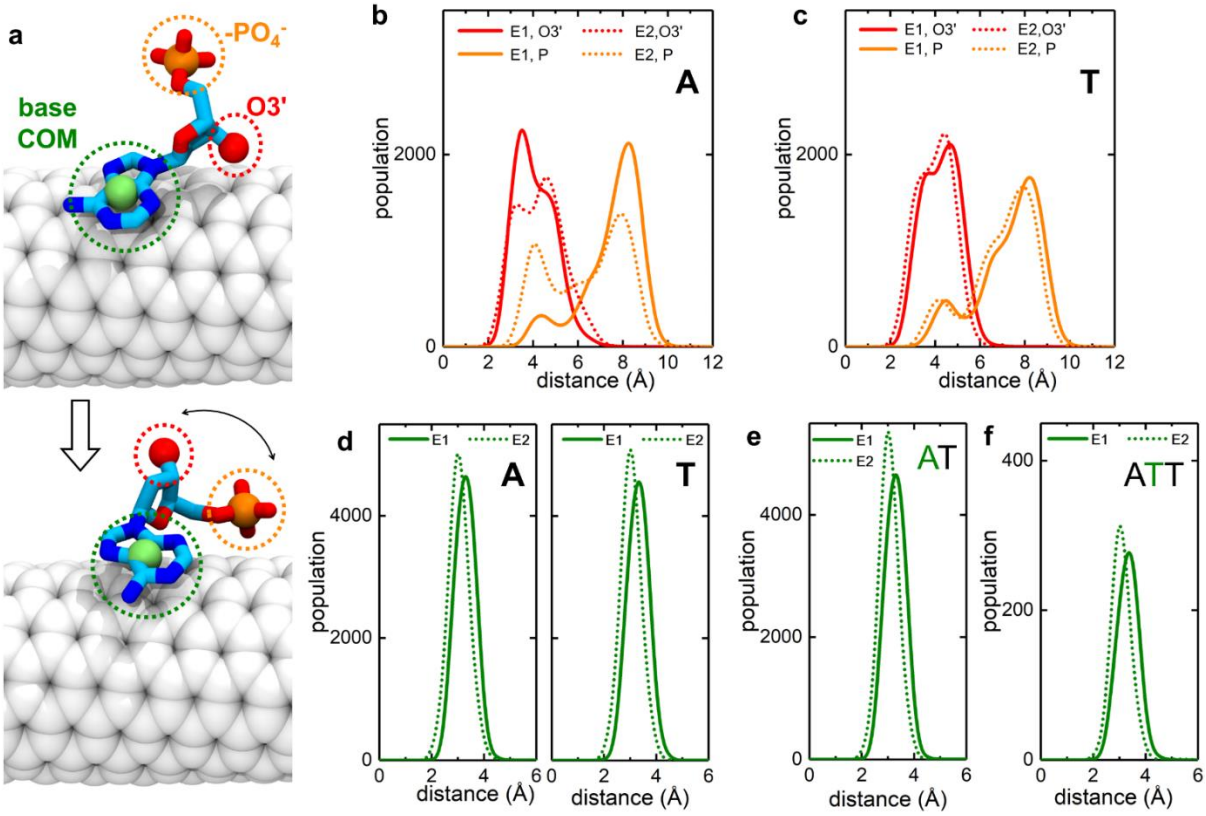

Figure 1. Binding modes and distances between nucleotides and surfaces of SWNT enantiomers. a) Snapshots of two representative binding modes for A nucleotide at the (7,5) SWNT surface. SWNT atoms are shown as white spheres, and DNA heavy atoms are colored in light blue (C), dark blue (N), red (O) and orange (P). Hydrogen atoms are not shown for clarity. The center of mass of the base is shown as a green sphere. b) Distribution of distances between phosphate groups or O3' atoms and SWNT surfaces, determined for A nucleotide binding to two enantiomers of (7,5) SWNT. c) Distribution of distances between phosphate groups or O3' atoms and SWNT surfaces, determined for T nucleotide binding to two enantiomers of (7,5) SWNT. d) Distribution of distances between base centers of mass and SWNT surfaces, determined for single A and T nucleotides binding to two enantiomers of (7,5) SWNT. e) Distribution of distances between base COMs and SWNT surfaces, determined for A nucleotide in AT molecule binding to two enantiomers of (7,5) SWNT in a 1 μs trajectory. f) Distribution of distances between base COMs and SWNT surfaces, determined for the second nucleotide in the ATT molecule binding to two enantiomers of (7,5) SWNT, extracted from every hundredth frame of ~6 μs long trajectory.

Stacking of DNA Nucleotides on SWNT Enantiomers. To determine if there are fundamental differences in binding of DNA, a chiral molecule, to two enantiomers of the same type of carbon nanotube, we first examine binding of the simplest DNA molecules, i.e., single nucleotides, to enantiomers of (7,5) SWNTs using atomistic MD simulations. (7,5) SWNT chirality was chosen because previous spectroscopic and kinetic studies demonstrated that $(ATT)_4$ DNA molecules bind with different affinity to two enantiomers of (7,5) SWNT and lead to different coating coverage of these enantiomers[26,27]. In general, kinetic stability of short oligonucleotides on SWNTs was shown to be sequence-dependent[30].

A typical binding mode of a nucleotide to the SWNT surface is shown for adenine (A) in **Figure 1a,** and similar modes are observed for thymine (T), cytosine (C) and guanine (G). The nucleotide base always

stacks on the SWNT surface, while sugar and phosphate backbone are lifted away from the SWNT surface in either of two major conformations. In one conformation, the O3' atom of the sugar points towards the SWNT surface and the phosphate group dangles in the aqueous solution, whereas in the other conformation, the O3' side of the sugar lifts into the solution, bringing the phosphate group nearer the SWNT surface.

To quantify nucleotide conformational preferences on two SWNT enantiomers, we obtained the distribution of distances of sugar and phosphate groups from the SWNT surface, as shown in **Figure 1b,c**. The plots show distributions for A and T binding to two (7,5) SWNT enantiomers in 1 μs long simulations. Two (7,5) SWNT enantiomers, visually distinguishable in simulations, are referred to as E1 and E2. The enantiomers E1 and E2 correspond to what are typically called *M* and *P* SWNT enantiomers with chiral index (7,5) (**Figure S1**). In **Figure 1b**, the O3' atom of the sugar of A-nucleotide is shown to always stay within 6 Å of the SWNT surface for both (7,5) enantiomers. However, there is a preference for O3' to be closer to the SWNT surface for enantiomer E1 (at ~3.3 Å distance), than for E2 (at ~4.5 Å distance). For phosphate group, there is a clear difference when adenine is binding to two enantiomers; phosphate group remains predominantly far away from E1 surface (at 8.3 Å), whereas while binding to E2, its distance is ~40% of the time at 4 Å and ~60% of the time further at 8 Å from E2 surface. Therefore, adenine shows quite different preferences in sugar and phosphate group distances and orientations from E1 and E2 surfaces. In contrast, the plots of O3' and P-atom distances show little differences when thymine is binding to two enantiomers of (7,5) SWNTs, as shown in **Figure 1c**. However, interestingly, the phosphate group and O3' distance distribution plots for T are consistently shifted to the left by ~0.3 Å (to closer distances) when T is at the surface of E2.

Next, we quantified the distances of the centers of mass (COMs) of nucleotide bases from surfaces of two SWNT enantiomers, shown in **Figure 1d**. Notably, the bases of both single nucleotides A and T prefer stacking nearer to the surface of the E2 enantiomer than to the surface of the E1 enantiomer. The distance distributions are again consistently shifted to the left by ~0.5 Å for the E2 enantiomer, compared to the E1 enantiomer. The shifts observed in **Figure 1b-e** are consistent with the results of the second independent runs for the examined systems (**Figure S2a-b**). Furthermore, the bases of single nucleotides G and C also consistently stack closer to the E2 SWNT surface on average, as seen in **Figure S2c-d**. The shifts in COM distance distributions are also observed for polynucleotide molecules AT and ATT binding to (7,5) SWNT enantiomers, as shown for two representative nucleotide bases in **Figure 1e-f** and for all the bases in the studied oligonucleotides in **Figure S3**. These base shifts were also reproduced in *ab initio* MD simulations of nucleotide A binding to SWNT enantiomers E1 and E2 (**Figure S4**). Separate quantum calculations of nucleotide A binding to E1 and E2 SWNT enantiomers in the gas phase also reveal that the binding affinity of A is stronger for E2, with a binding energy value of -29.0 kcal/mol, than for E1, with a binding energy of -26.4 kcal/mol (**Figure S5**).

Orientations of DNA Nucleotides on (7,5) SWNT Enantiomers. The key difference between two SWNT enantiomers, which are mirror images of each other, is the tilt of the benzene rings in the nanotube structure. Since single DNA nucleotides have inherent chirality to them, we hypothesized that single nucleotides may favor different orientations with respect to the SWNT long axis, when binding to nanotube enantiomers. The orientations (angles) of stacked nucleotides with respect to the SWNT are defined in Methods and depicted in **Figures 2a** and **S6**. The orientation of the nucleotide base is defined by the angle θ, which lies in a two-dimensional plane defined by x' and z' axes, which cross at the COM of the nucleotide base. This angle θ, with the range from 0° to 360°, measures the orientation of the stacked nucleotide base in the plane that is tangential to the SWNT surface.

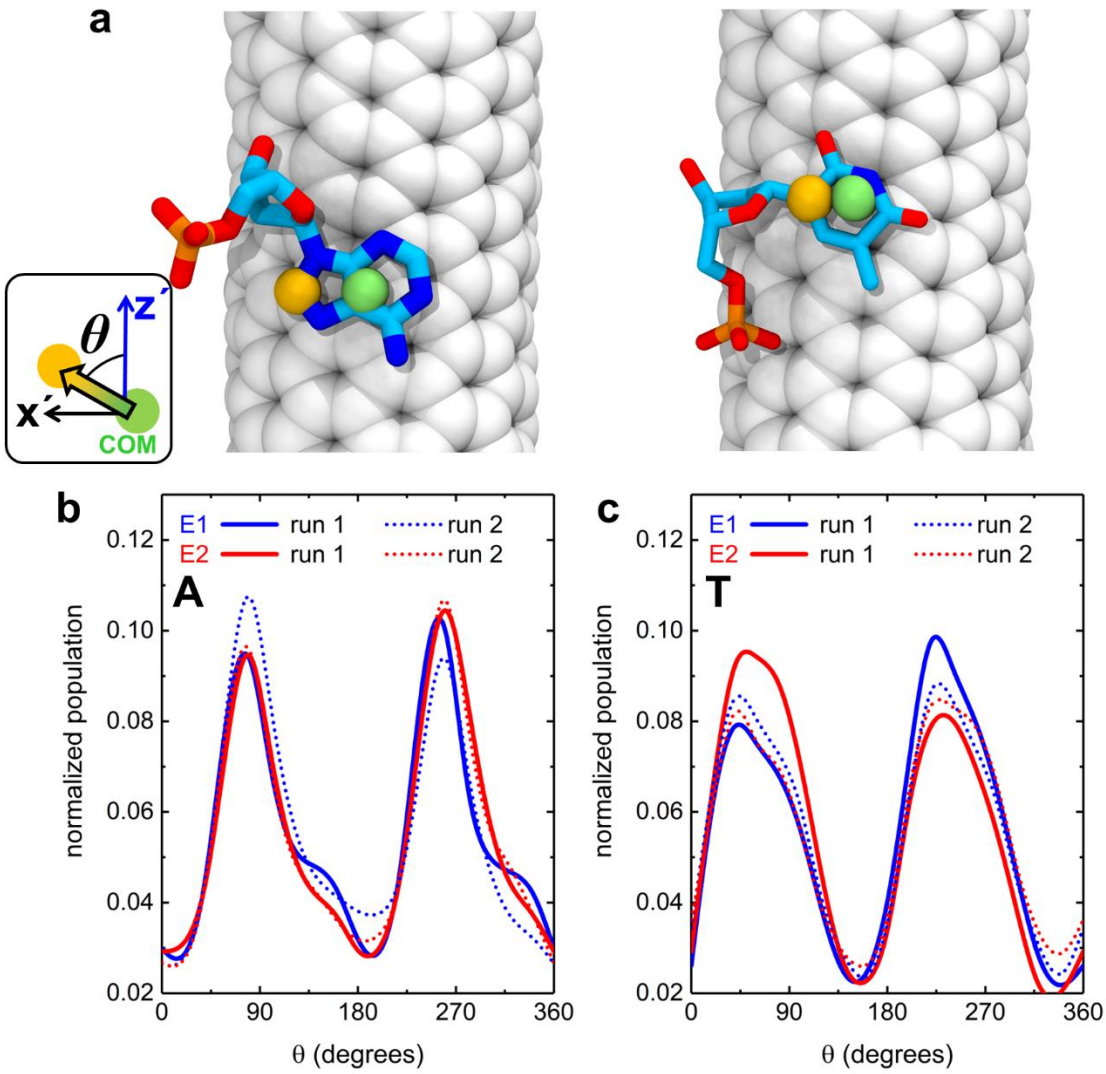

Figure 2. Orientations of single nucleotides on surfaces of (7,5) SWNT enantiomers. a) A and T nucleotides in orientations with $\theta \sim 90°$ on the E1 nanotube surface. The color scheme is consistent with the scheme used above. The green sphere is the nucleotide base COM, and the yellow sphere is the edge atom of the base used to calculate the base vector. b) Distribution of θ angles that the base of the A nucleotide makes with respect to the z' axis, evaluated for simulations of a single A nucleotide binding to two enantiomers of (7,5) SWNT. c) Distribution of θ angles that the base of the T nucleotide makes with respect to the z' axis, evaluated for simulations of a single T nucleotide binding to two enantiomers of (7,5) SWNT.

Figures 2b-c show the distribution of θ for A and T nucleotides stacking on E1 and E2 enantiomers, measured during two independent 1 μs-long simulations. For both A and T, two distinct preferred orientations are observed. For A, preferred values of θ are at ~75-77° and 255-260°. For T, there is a broad peak with a shoulder at 45° that broadens all the way to 70°, and another peak centered between 220° and 230°. The preferred values of the angle are consistent between the independent runs, indicating the reproducibility of the results. Contrary to our expectations, plots in **Figures 2b-c** show that A and T nucleotides have almost no differences in their preferred orientations on SWNT surface when binding to E1 and E2 enantiomers.

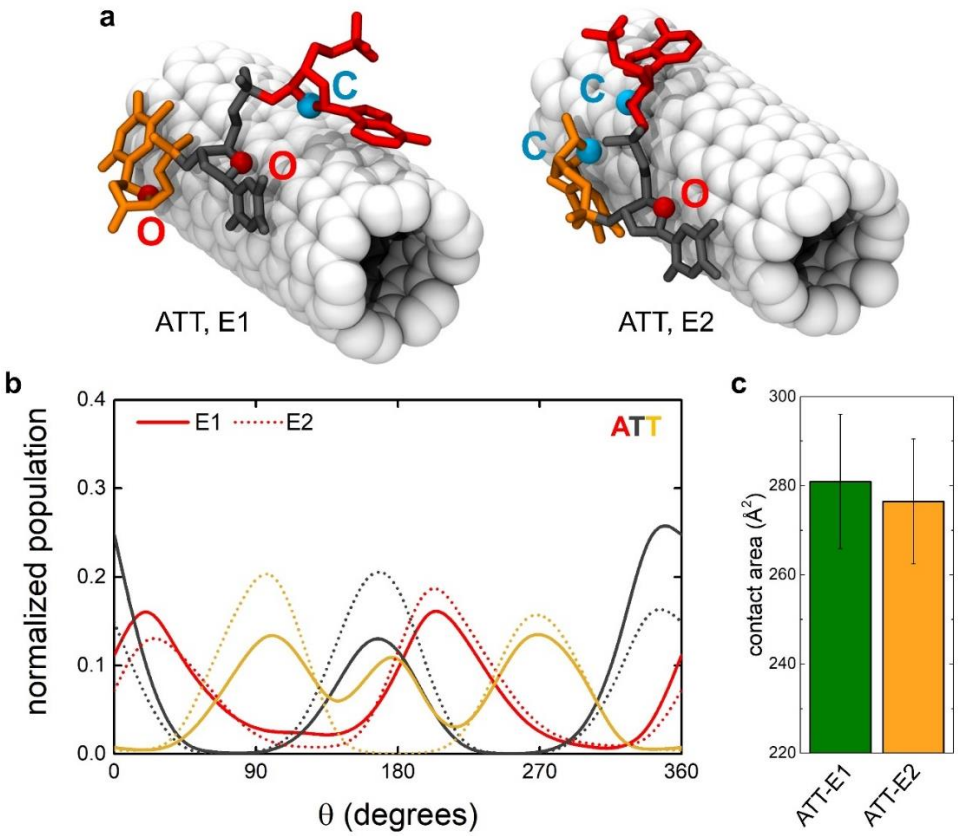

Figure 3. Characterization of ATT binding to (7,5) SWNT enantiomers. a) Representative snapshots of ATT conformations, when binding to E1 and E2 SWNT enantiomers. Nucleotides A, T, and T are shown in red, grey, and orange respectively. The C2' atom is highlighted in cyan and the O4' atom is highlighted in red, when pointing towards the SWNT surface. b) Distribution of θ angles that the bases of ATT molecule make with respect to the z' axis, evaluated for simulations of the ATT molecule binding to two enantiomers of (7,5) SWNT. c) Contact areas between the whole ATT molecules and the surfaces of E1 and E2 SWNT enantiomers. Plots in panels b-c were obtained from ~6 μs-long simulations.

Interactions of AT and ATT DNA Oligonucleotides with SWNT Enantiomers. Apart from the observation that all the nucleotide bases consistently stack closer to the surface of the E2 enantiomer than the E1 enantiomer (**Figure 1**), no other significant differences were observed for the binding of AT oligonucleotide to the SWNT enantiomers (**Figure S7**). Next, we examined ATT binding to E1 and E2 enantiomers, whose representative binding modes are shown in **Figure 3a**. Our simulations revealed that the nucleotide sugar backbone can assume different orientations when ATT is binding to E1 or E2 enantiomer. For example, when ATT binds to the E1 enantiomer, sugar moieties of nucleotides point C2' (A), O4' (T), and O4' (T) atoms towards the SWNT surface during the initial ~2 μs length of the trajectory. On the other hand, when ATT binds to the E2 enantiomer, sugar moieties of nucleotides point C2' (A), O4' (T), and C2' (T) atoms to the SWNT surface throughout the trajectory. After the initial ~2 μs, sugars of the ATT backbone started facing the surface of E1 enantiomer with C2' (A), O4' (T), and C2' (T) atoms i.e., in a similar manner as when binding to the E2 enantiomer (**Figure S8**).

To quantify the differences of ATT binding to E1 and E2 enantiomers, we also examined the distributions of θ angles that ATT bases make with respect to the long axis of the nanotube. The plot in **Figure 3b** shows the distribution of θ for all three (ATT) bases stacking on the surfaces of two SWNT enantiomers. Here, it is observed that T3 has a difference in preferred θ values when binding to the surface of SWNT enantiomers E1 and E2. The first nucleotide A has preferred θ values of ~20°-40° and ~200°-240° and the

second nucleotide T shows preferred θ values of ~0°-20°, ~140°-190° and ~320°-340° for both E1 and E2 enantiomers. The third nucleotide T shows preferred θ values of ~80°-120° and ~240°-300° when binding to both E1 and E2, but it also has an additional preferred θ value of ~180° when binding to the E1 enantiomer only. This difference in preferred θ values of the third nucleotide T, was, however, not reproducible in a second independent ~6 µs trajectory simulation of ATT-SWNT conjugates (**Figure S9**), indicating that ATT molecules have a complex conformational space when binding to SWNT surfaces.

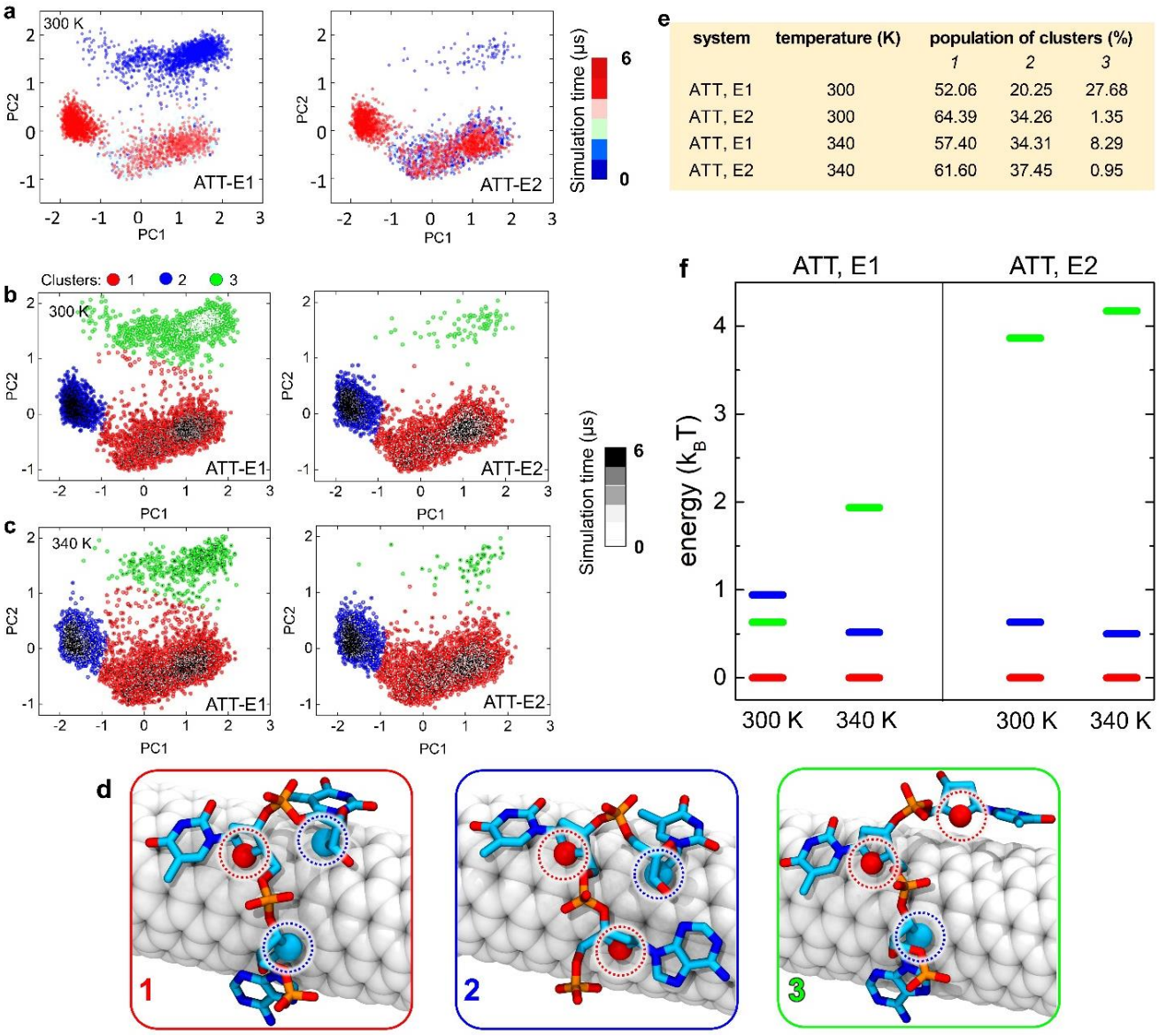

system	temperature (K)	population of clusters (%)		
		1	*2*	*3*
ATT, E1	300	52.06	20.25	27.68
ATT, E2	300	64.39	34.26	1.35
ATT, E1	340	57.40	34.31	8.29
ATT, E2	340	61.60	37.45	0.95

Figure 4. PCA and clustering analysis of ATT conformations on (7,5) SWNT enantiomers. a) PCA analysis of ATT conformations on E1 and E2 enantiomers at 300 K, with points colored according to trajectory time. b) Clustering analysis of PCA maps of ATT conformations on E1 and E2 enantiomers at 300 K, using Gaussian mixture method. c) Clustering analysis of PCA maps of ATT conformations on E1 and E2 enantiomers at 340 K, using Gaussian mixture method. d) Snapshots of central structures of each cluster shown in panel b for ATT molecule adsorbed on the surface of E1 enantiomer. The key differences between conformations in three clusters are orientations of sugars with respect to the SWNT surface. e) Populations of clusters shown in panels b and c. f) Energy differences between conformational states (clusters), obtained using the Boltzmann equation.

We also examined the contact areas that ATT nucleotides make with E1 and E2 enantiomers. During ~6 μs trajectory, ATT was found to have a higher contact area with E1 (~281 Å) than with E2 (~276 Å), as shown in **Figure 3b**. These results indicate that the orientation of the nucleotide sugar backbone on the SWNT surface can affect the total contact area that oligonucleotides make with the SWNT surface.

Principal Component Analysis and Clustering of ATT Conformations on SWNT Enantiomers. To better examine the conformational space of ATT molecule on two SWNT enantiomers, we analyzed ~6 μs long trajectories of ATT molecules binding to two (7,5) SWNT enantiomers with the principal component analysis (PCA), shown in **Figure 4a**. The PCA maps indicate that ATT molecules have three dominant conformations, represented by three main clusters. To determine the number of conformations contributing to each cluster, a clustering analysis was performed on the maps using the Gaussian mixture method. The results of the clustering analysis for ATT molecules binding to two (7,5) SWNT enantiomers, simulated at both 300 K and 340 K temperatures, shown in **Figures 4b-c**, **S10**, and **S11**, demonstrate that ATT molecule populates two conformations with similar frequency when binding to E1 and E2 enantiomers, as confirmed in the data of **Figure 4e**. However, the population of the third conformation is significantly higher when ATT is binding to E1, when between 8 % and 28% of all molecules assume the third conformation, than when ATT is binding to E2, for which ~1% of all molecules assume the third conformation. Interestingly, the clusters correspond to distinct conformations of ATT molecule when binding to the SWNT surfaces. The main difference in conformations is the orientation of the sugar moieties of three nucleotides with respect to the SWNT surfaces, highlighted in **Figure 4d**. For example, the structures in the first cluster have sugar C2' (A), O4' (T), and C2' (T) atoms oriented towards the SWNT surface. In the second cluster, the sugar atoms pointing towards the SWNT surface are O4' (A), O4' (T), and C2' (T), whereas in the third cluster, the atoms are C2' (A), O4' (T), and O4' (T). Snapshots of central structures of all clusters from all the ATT simulations performed are shown in **Figures S12-S13**. We note that the binding pose of ATT when its sugar atoms C2' (A), O4' (T), and O4' (T) point towards the E1 SWNT surface for ~2 μs of the trajectory corresponds to the ATT conformation found in the third (green) cluster, which is more prominent in ATT conjugates with E1 enantiomer.

Using the Boltzmann distribution and the population analysis, we obtained a diagram of energies of three major conformations for ATT molecules binding to two (7,5) SWNT enantiomers, simulated at both 300 K and 340 K temperatures, shown in **Figure 4f**. This figure confirms that the energy of the third major conformation of ATT is one distinguishing feature for this molecule binding to E1 and E2 enantiomers. The energy of the third conformation of ATT is ~2-3 k_BT higher for E2 than for E1.

Conclusion

In this work we investigated the binding between two SWNT enantiomers to single nucleotides A, T, C, G, to AT dinucleotide and to ATT trinucleotide using classical atomistic MD simulations. Two enantiomers are mirror images of each other and differ in the tilt of the benzene rings which are wrapped to form the nanotubes. We consistently observed that on average all the nucleotide bases stack closer to the surface of the E2 enantiomer than to the surface of the E1 enantiomer. Contrary to our expectations, chiral single DNA nucleotides and AT molecules did not show enantiomer-dependent preferences in angular orientations with respect to the SWNT long axis.

ATT molecules were found to have some differences in preferred orientations on surfaces of two SWNT enantiomers. In addition to differing orientations, ATT molecules also had different arrangements of sugar atoms facing the surfaces of SWNT enantiomers. To better examine the conformations of ATT molecules on SWNT enantiomers, we examined the trajectories using the principal component analysis and clustering

analysis. These analyses showed that ATT molecules have three principal conformations when binding to SWNT enantiomers. These conformations differ in the arrangements of sugar atoms facing the SWNT surfaces. While two conformational states of ATT had similar populations in the presence of both E1 and E2 enantiomers, the third conformational state of ATT was significantly more populated for E1 than for E2. The differences in populations of the third cluster agree with the results from simulations of ATT systems at a higher temperature, 340 K.

Overall, our simulations demonstrate that three nucleotide-long ssDNA molecules start showing differences when binding to SWNT enantiomers. The binding mode differences include angular orientations of DNA bases with respect to the SWNT long axis, and preferred arrangements of the sugar atoms contacting the SWNT surface. Previous studies[27] identified the right-handed SWNT isomer as the species with higher DNA binding affinity and designated contact area as the key parameter helping DNA to sort between SWNT enantiomers. According to these studies, contact area has been identified as the useful parameter to describe surface coverage differences between different DNA structures with one desorbed base, partially desorbed base or two desorbed bases. Based on our results, we identify the preferred arrangements of the DNA sugar moieties as another important parameter that can contribute to different binding of same DNA molecules to chiral SWNT enantiomers. Our observations could be related to the fact that the chirality of nucleic acids originates in the configurational asymmetry of sugar moieties, which constitute the nucleic acid backbone.[31] Overall, our results take us one step further towards understanding how ssDNA nucleotides differentiate between enantiomers of SWNTs of the same chirality.

Methods

Atomistic Models of DNA-SWNT Systems. Two segments of (7,5) single-walled carbon nanotube enantiomers, 4 nm in length, were built with the *Carbon Nanostructure Builder* plugin in VMD software[32]. The initial coordinates of all single nucleotides (A, T, C, and G) and polynucleotides (AT and ATT) were obtained by extracting their coordinates from several crystal structures found at the RCSB Protein Data Bank[33]. Each type of DNA molecule was positioned within 5 Å from the outer SWNT surface, at midpoint along the SWNT length, using our own tcl script. All the DNA-SWNT systems were solvated and neutralized in 0.1 M NaCl aqueous solution with TIP3P water model, using *solvate* and *ionize* VMD plugins. Numbers of atoms in all the built systems are summarized in **Table S1.**

Classical Molecular Dynamics Simulations. Atomistic simulations were performed to investigate two enantiomers of (7,5) SWNTs interacting with single, di- and tri- nucleotides. The systems were described with CHARMM36 force field parameters[34,35] and the simulations were performed with NAMD2.13 package[36]. All simulations were conducted with Langevin dynamics in the NpT ensemble, where the value of the Langevin constant γ_{Lang} was set at 1.0 ps^{-1}, the pressure remained constant at 1 bar, at the temperature remained constant at either 298 K or 340 K. The time step was set to 2.0 fs, and the van der Waals and short-range Coulomb interactions were calculated every 1 and 2 time steps, respectively, using 12 Å as a cutoff distance. The long-range Coulomb interactions were calculated every 2 time steps using the Particle Mesh Ewald (PME) method[37], with periodic boundary conditions applied in all directions. After 2,000 steps of minimization, solvent molecules were equilibrated for 0.1 ns around the DNA-SWNT conjugate. The atoms of this conjugate were restrained using harmonic forces with a spring constant of 1 kcal (mol·Å)$^{-1}$. Next, the systems were equilibrated in production MD runs, with harmonic restraints applied on the nucleotides with a spring constant of 1 kcal (mol·Å)$^{-1}$. The lengths of all simulations are summarized in **Table S1.**

Contact Area Calculations. Contact areas between DNA nucleotides (whole or its selected parts) and SWNT surface at time *t,* $s_{contact\ area}\ (t)$, were calculated based on the following equation

$$s_{contact\ area}\ (t) = \frac{s_{SWNT}(t) + s_{DNA}(t) - s_{SWNT\ and\ DNA}(t)}{2} \qquad (1)$$

where $s_{SWNT}(t)$ and $s_{DNA}(t)$ are the solvent accessible surface areas (SASA) of SWNT and selected DNA atoms at time t, respectively. $s_{SWNT\ and\ DNA}(t)$ represents SASA of SWNT and selected DNA atoms altogether. The contact areas were calculated for all nucleotide types binding to SWNT enantiomers with SASA VMD plugin, where, the van der Waals radius of atoms was defined as 1.4 Å to designate the points on a sphere which are accessible to the solvent.

Calculations of Nucleotide Base Orientations on SWNT Surface. Next, we defined the angle θ which a nucleotide base, adsorbed on the outer SWNT surface, makes with respect to the long axis of the SWNT. We calculate θ using the equations given below, as implemented in our Fortran code. This angle θ, spanning the range from 0° to 360°, is defined in a plane shown in red color in **Figure S6a**. For convenience, all points in the red plane will be defined using new Cartesian axes x' and z'. The equations of the red plane, and x' and z' axes depend on the coordinates of the center of mass (COM) of the nucleotide base, which are, in turn, dependent on time. The red plane is tangential to the nanotube surface, and it passes through the base COM, whose coordinates at a given time are labeled as (x_A, y_A, z_A). The equation of this red plane at that point in time is defined as:

$$2x_A(x - x_A) + 2y_A(y - y_A) = 0 \qquad (2)$$

By rearranging and simplifying this equation, we rewrite the equation of the red plane as:

$$ax + by = d \qquad (3)$$

where $a=2x_A$, $b=2y_A$, $d=2(x_A^2+y_A^2)$. Next, we also define a new plane which is perpendicular to the red plane and which also passes through the base COM, whose equation is:

$$z = z_A = c \quad (4)$$

This second plane is shown in green in **Figure S6a.**

Equations 2-4 are next used to define the x' and z' axes. The x' axis is defined as the intersection line between the red and green planes in **Figure S6a**. The equation of the x' line can be obtained as a vector difference between two points with arbitrarily chosen values of the parametrization constant t (in our code, set to $t = 10$ and 20):

$$x' = t\hat{\imath} + \left(\frac{d}{b} - \frac{a}{b}t\right)\hat{\jmath} + c\hat{k} \qquad (5)$$

As a vector, the x' line can have two possible directions, so we added special criteria to define the direction in our code. By these criteria, the direction of the x' axis is determined by the quadrant in which the base COM lies in the (x,y) plane, as shown schematically in **Figure S6c**.

The second axis that defines the red plane is the z' axis, which passes through the red plane and is parallel to the original z axis of the system. The z' axis is defined as a vector difference between two points with arbitrarily chosen values of the parametrization constant u (in our code, set to $u = 10$ and 20):

$$z' = x_A\hat{\imath} + y_A\hat{\jmath} + (z_A + u)\hat{k} \qquad (6)$$

Finally, θ is the angle between the vector which describes the nucleotide base, $\vec{P}$, and the z' axis, as shown in **Figure S6b**. The vector $\vec{P}$ has the base COM as its starting point, and a selected edge atom of the base as its ending point. Our tcl script evaluates the angle θ as the angle which $\vec{P}$ makes with the z' axis, by using the *atan2* function, whose result we express in the range from 0° to 360°.

Distance Calculations. To quantify the binding between different DNAs and SWNT enantiomers, we calculated distances between selected atoms of DNA nucleotides (base, phosphate group, sugar backbone atoms, or other selections), and the SWNT surface at time t:

$$d(t) = r_{DNA}(t) - r_{SWNT} \qquad (7)$$

where $r_{DNA}(t)$ is the radial distance of the center of mass of the selected DNA atoms at time t, defined in the cylindrical coordinate system and r_{SWNT} is the radius of the (7,5) SWNT.

Principal Component Analysis. PCA is a widely used multivariate analysis tool to compress and extract key features from high-dimensional data for easier interpretation. PCA can reduce the information contained in MD trajectories of biological macromolecules and allow the interpretation of the essential dynamics between conformational states of these molecules[38–40]. Here, the ensembles of structures of ATT DNAs binding to two SWNT enantiomers is analyzed with PCA implemented in the Gromacs software[41].

First, all the trajectories of ATT molecules bound to two SWNT enantiomers, simulated at 300 K and 340 K temperatures, were concatenated into a single trajectory using the *catdcd* module. The coordinates of all atoms in ATT molecules from all simulations, aligned with respect to the initial (reference) structure, were used to construct the positional covariance matrix. PCA was then carried out by diagonalizing this matrix and obtaining its eigenvectors and eigenvalues, which represent the modes and amplitudes of the collective motions in ATT molecules, respectively. Coordinates of ATT molecules from separate trajectories were projected on the obtained eigenvectors to help us understand the conformational space of these molecules.

Clustering Analysis of Two-Dimensional PCA Maps. Two-dimensional PCA maps of trajectories of ATT molecules binding to two SWNT enantiomers at 300 K and 340 K showed three distinct clusters, which we analyzed with the clustering analysis using the Gaussian mixture method. The Gaussian mixture clustering was performed with a Python code adapted from the *BinderSpace* package[42], where the number of components was set to 3 and the traditional k-means clustering algorithm was used to generate the initial centers for the model components.

With clustering analysis, all trajectory points were assigned to clusters, where each cluster represents a distinct conformational state of the system. The cluster populations were counted, and these populations were used to determine energy differences between clusters via the Boltzmann distribution:

$$\frac{N_i}{N_j} = e^{\epsilon_j - \epsilon_i / k_B T} \qquad (10)$$

where N_i and N_j are populations and ϵ_i and ϵ_j are the absolute energies of clusters i and j, k_B is the Boltzmann constant, and T is temperature.

The central structures from all the clusters in PCA maps, as determined using the Gaussian mixture method, were obtained using the gmx cluster tool in GROMACS[41].

QM/MD Simulations. We performed quantum mechanics / molecular dynamics (QM/MD) simulations of two systems, including a single A nucleotide interacting with either one of two enantiomers of (7,5) SWNT, and solvated by a single Na^+ ion and a spherical bubble of water with radius of 2.8 nm. In these simulations, SWNT, DNA and Na^+ ion were described quantum mechanically and water was described classically using the TIP3P model. The initial structures were extracted from the systems equilibrated in classical MD simulations. In the selected structures, the initial orientations of the nucleotide with respect to the long axis of SWNT, mathematically defined in the angle analysis section below, corresponded to the angles of 80° and 200°. These values of angles between nucleotide and SWNT axis corresponded to the highest populated (80°) and least populated (200°) angle conformers of A nucleotide, as shown in the angle

distribution plots in **Figure 2b.** The QM/MD simulations were carried out using the TeraChem software[43]. Initially, the quantum parts of the system were described at the ωB97X/sto-3g level, with dispersion corrections (DFT-D2). Single point energy calculations were run for 100 steps at 310 K with each time step being equal to 1 fs. After the initial 100 steps, a follow up 1 ps-long simulation (1,000 steps) was run at the temperature of 310 K, while describing the quantum parts of the system at the ωB97X/3-21G* level, which were used previously to describe DNA-SWNT conjugates[44].

Quantum Chemical Calculations. All quantum chemical calculations were performed with the Gaussian program package[45] using the M05-2X functional[46] in conjunction with the 3-21G basis set [47,48]. This level of theory was recently employed for analysis of complexes formed by binding porphyrin to SWNTs[49]. Frequency calculations confirmed that all optimized species represent minima on the corresponding potential energy surfaces. The binding energies were computed by subtracting electronic energies of the optimized nanotubes and nucleotide A from the energy of the complex.

Acknowledgments. We acknowledge the support of the NSF CBET-2106587 award (to L.V.), the computer time provided by the Texas Advanced Computing Center (TACC), and the Ministry of Science, Technological Development and Innovation of the Republic of Serbia within the framework of contract number 451-03-47/2023-01/200146 (to M.P.).

References

(1) Barone, P. W.; Baik, S.; Heller, D. A.; Strano, M. S. Near-Infrared Optical Sensors Based on Single-Walled Carbon Nanotubes. *Nature Materials*. Nature Publishing Group 2005, pp 86–92. https://doi.org/10.1038/nmat1276.

(2) Kang, S. J.; Kocabas, C.; Ozel, T.; Shim, M.; Pimparkar, N.; Alam, M. A.; Rotkin, S. V.; Rogers, J. A. High-Performance Electronics Using Dense, Perfectly Aligned Arrays of Single-Walled Carbon Nanotubes. *Nat Nanotechnol* **2007**, *2* (4), 230–236. https://doi.org/10.1038/nnano.2007.77.

(3) Odom, T. W.; Huang, J. L.; Kim, P.; Lieber, C. M. Structure and Electronic Properties of Carbon Nanotubes. *Journal of Physical Chemistry B* **2000**, *104* (13), 2794–2809. https://doi.org/10.1021/jp993592k.

(4) White, C. T.; Mintmire, J. W. Fundamental Properties of Single-Wall Carbon Nanotubes. *Journal of Physical Chemistry B*. January 13, 2005, pp 52–65. https://doi.org/10.1021/jp047416.

(5) Jhon, Y. I.; Kim, C.; Seo, M.; Cho, W. J.; Lee, S.; Jhon, Y. M. Tensile Characterization of Single-Walled Carbon Nanotubes with Helical Structural Defects. *Sci Rep* **2016**, *6*. https://doi.org/10.1038/srep20324.

(6) Ackermann, J.; Metternich, J. T.; Herbertz, S.; Kruss, S. Biosensing with Fluorescent Carbon Nanotubes. *Angewandte Chemie - International Edition*. John Wiley and Sons Inc April 25, 2022. https://doi.org/10.1002/anie.202112372.

(7) Agarwal, S.; Kallmyer, N. E.; Vang, D. X.; Ramirez, A. V.; Islam, M. M.; Hillier, A. C.; Halverson, L. J.; Reuel, N. F. Single-Walled Carbon Nanotube Probes for the Characterization of Biofilm-Degrading Enzymes Demonstrated against Pseudomonas Aeruginosa Extracellular Matrices. *Anal Chem* **2022**, *94* (2), 856–865. https://doi.org/10.1021/acs.analchem.1c03633.

(8) Zhang, J.; Kruss, S.; Hilmer, A. J.; Shimizu, S.; Schmois, Z.; De La Cruz, F.; Barone, P. W.; Reuel, N. F.; Heller, D. A.; Strano, M. S. A Rapid, Direct, Quantitative, and Label-Free Detector of Cardiac Biomarker Troponin T Using Near-Infrared Fluorescent Single-Walled Carbon Nanotube Sensors. *Adv Healthc Mater* **2014**, *3* (3), 412–423. https://doi.org/10.1002/adhm.201300033.

(9) Kelich, P.; Jeong, S.; Navarro, N.; Adams, J.; Sun, X.; Zhao, H.; Landry, M. P.; Vuković, L. Discovery of DNA-Carbon Nanotube Sensors for Serotonin with Machine Learning and Near-Infrared Fluorescence Spectroscopy. *ACS Nano* **2022**, *16* (1), 736–745. https://doi.org/10.1021/acsnano.1c08271.

(10) Yadav, A.; Kelich, P.; Kallmyer, N.; Reuel, N. F.; Vuković, L. Characterizing the Interactions of Cell-Membrane-Disrupting Peptides with Lipid-Functionalized Single-Walled Carbon Nanotubes. *ACS Appl Mater Interfaces* **2023**, *15* (20), 24084–24096. https://doi.org/10.1021/acsami.3c01217.

(11) Yang, F.; Wang, M.; Zhang, D.; Yang, J.; Zheng, M.; Li, Y. Chirality Pure Carbon Nanotubes: Growth, Sorting, and Characterization. *Chemical Reviews*. American Chemical Society March 11, 2020, pp 2693–2758. https://doi.org/10.1021/acs.chemrev.9b00835.

(12) Yang, X.; Tan, H.; Yuan, M.; Zhou, Y.; Cao, M.; Zhang, H.; Hu, P.; Zhang, M. Introducing Chirality Concept of Single-Walled Carbon Nanotubes to High School Students and Undergraduates by Paper Origami in Their Science Projects. *J Chem Educ* **2021**. https://doi.org/10.1021/acs.jchemed.1c01208.

(13) Qiu, L.; Ding, F. Understanding Single-Walled Carbon Nanotube Growth for Chirality Controllable Synthesis. *Acc Mater Res* **2021**, *2* (9), 828–841. https://doi.org/10.1021/accountsmr.1c00111.

(14) Komatsu, N. Stereochemistry of Carbon Nanotubes. *Jpn J Appl Phys* **2010**, *49* (2 PART 2). https://doi.org/10.1143/JJAP.49.02BC01.

(15) Charoenpakdee, J.; Suntijitrungruang, O.; Boonchui, S. Chirality Effects on an Electron Transport in Single-Walled Carbon Nanotube. *Sci Rep* **2020**, *10* (1). https://doi.org/10.1038/s41598-020-76047-9.

(16) Kayang, K. W.; Banna, A. H.; Volkov, A. N. Chirality-Dependent Mechanical Properties of Bundles and Thin Films Composed of Covalently Cross-Linked Carbon Nanotubes. *Langmuir* **2022**, *38* (6), 1977–1994. https://doi.org/10.1021/acs.langmuir.1c02632.

(17) Matsukawa, Y.; Umemura, K. Chirality Luminescent Properties of Single-Walled Carbon Nanotubes during Redox Reactions. *Opt Mater (Amst)* **2021**, *112*. https://doi.org/10.1016/j.optmat.2020.110748.

(18) Rajter, R. F.; French, R. H.; Ching, W. Y.; Podgornik, R.; Parsegian, V. A. Chirality-Dependent Properties of Carbon Nanotubes: Electronic Structure, Optical Dispersion Properties, Hamaker Coefficients and van Der Waals-London Dispersion Interactions. *RSC Adv* **2013**, *3* (3), 823–842. https://doi.org/10.1039/c2ra20083j.

(19) Li, H.; Sims, C. M.; Kang, R.; Biedermann, F.; Fagan, J. A.; Flavel, B. S. Isolation of the (6,5) Single-Wall Carbon Nanotube Enantiomers by Surfactant-Assisted Aqueous Two-Phase Extraction. *Carbon N Y* **2023**, *204*, 475–483. https://doi.org/10.1016/j.carbon.2022.12.071.

(20) Ao, G.; Khripin, C. Y.; Zheng, M. DNA-Controlled Partition of Carbon Nanotubes in Polymer Aqueous Two-Phase Systems. *J Am Chem Soc* **2014**, *136* (29), 10383–10392. https://doi.org/10.1021/ja504078b.

(21) Tu, X.; Manohar, S.; Jagota, A.; Zheng, M. DNA Sequence Motifs for Structure-Specific Recognition and Separation of Carbon Nanotubes. *Nature* **2009**, *460* (7252), 250–253. https://doi.org/10.1038/nature08116.

(22) De Los Santos, Z. A.; Lin, Z.; Zheng, M. Optical Detection of Stereoselective Interactions with DNA-Wrapped Single-Wall Carbon Nanotubes. *J Am Chem Soc* **2021**, *143* (49), 20628–20632. https://doi.org/10.1021/jacs.1c11372.

(23) Ao, G.; Streit, J. K.; Fagan, J. A.; Zheng, M. Differentiating Left- and Right-Handed Carbon Nanotubes by DNA. *J Am Chem Soc* **2016**, *138* (51), 16677–16685. https://doi.org/10.1021/jacs.6b09135.

(24) Tu, X.; Zheng, M. A DNA-Based Approach to the Carbon Nanotube Sorting Problem. *Nano Res* **2008**, *1* (3), 185–194. https://doi.org/10.1007/s12274-008-8022-7.
(25) Lin, Z.; Yang, Y.; Jagota, A.; Zheng, M. Machine Learning-Guided Systematic Search of DNA Sequences for Sorting Carbon Nanotubes. *ACS Nano* **2022**, *16* (3), 4705–4713. https://doi.org/10.1021/acsnano.1c11448.
(26) Zheng, Y.; Bachilo, S. M.; Weisman, R. B. Enantiomers of Single-Wall Carbon Nanotubes Show Distinct Coating Displacement Kinetics. *Journal of Physical Chemistry Letters* **2018**, *9* (13), 3793–3797. https://doi.org/10.1021/acs.jpclett.8b01683.
(27) Zheng, Y.; Alizadehmojarad, A. A.; Bachilo, S. M.; Kolomeisky, A. B.; Weisman, R. B. Dye Quenching of Carbon Nanotube Fluorescence Reveals Structure-Selective Coating Coverage. *ACS Nano* **2020**, *14* (9), 12148–12158. https://doi.org/10.1021/acsnano.0c05720.
(28) Lee, O. S. How Does Ss-DNA Recognize the Chirality of Carbon Nanotubes? *J Comput Sci* **2016**, *15*, 60–64. https://doi.org/10.1016/j.jocs.2015.10.004.
(29) Roxbury, D.; Mittal, J.; Jagota, A. Molecular-Basis of Single-Walled Carbon Nanotube Recognition by Single-Stranded DNA. *Nano Lett* **2012**, *12* (3), 1464–1469. https://doi.org/10.1021/nl204182b.
(30) Alizadehmojarad, A. A.; Zhou, X.; Beyene, A. G.; Chacon, K. E.; Sung, Y.; Pinals, R. L.; Landry, M. P.; Vuković, L. Binding Affinity and Conformational Preferences Influence Kinetic Stability of Short Oligonucleotides on Carbon Nanotubes. *Adv Mater Interfaces* **2020**, *7* (15). https://doi.org/10.1002/admi.202000353.
(31) Winogradoff, D.; Li, P. Y.; Joshi, H.; Quednau, L.; Maffeo, C.; Aksimentiev, A. Chiral Systems Made from DNA. *Advanced Science*. John Wiley and Sons Inc March 1, 2021. https://doi.org/10.1002/advs.202003113.
(32) Humphrey, W.; Dalke, A.; Schulten, K. VMD: Visual Molecular Dynamics. *J. Mol. Graph.* **1996**, *14*, 33–38. https://doi.org/10.1016/0263-7855(96)00018-5.
(33) Berman, H. M.; Westbrook, J.; Feng, Z.; Gilliland, G.; Bhat, T. N.; Wissig, H.; Shindyalov, I. N.; Bourne, P. E. The Protein Data Bank. *Nucleic Acids Res* **2000**, *28* (1), 235–242. https://doi.org/10.1093/nar/28.1.235.
(34) Hart, K.; Foloppe, N.; Baker, C. M.; Denning, E. J.; Nilsson, L.; MacKerell, A. D. Optimization of the CHARMM Additive Force Field for DNA: Improved Treatment of the BI/BII Conformational Equilibrium. *J Chem Theory Comput* **2012**, *8* (1), 348–362. https://doi.org/10.1021/ct200723y.
(35) Huang, J.; Mackerell, A. D. CHARMM36 All-Atom Additive Protein Force Field: Validation Based on Comparison to NMR Data. *J. Comput. Chem.* **2013**, *34*, 2135–2145. https://doi.org/10.1002/jcc.23354.
(36) Phillips, J. C.; Hardy, D. J.; Maia, J. D. C.; Stone, J. E.; Ribeiro, J. V.; Bernardi, R. C.; Buch, R.; Fiorin, G.; Hénin, J.; Jiang, W.; McGreevy, R.; Melo, M. C. R.; Radak, B. K.; Skeel, R. D.; Singharoy, A.; Wang, Y.; Roux, B.; Aksimentiev, A.; Luthey-Schulten, Z.; Kalé, L. V.; Schulten, K.; Chipot, C.; Tajkhorshid, E. Scalable Molecular Dynamics on CPU and GPU Architectures with NAMD. *J. Chem. Phys.* **2020**, *153*, 044130-undefined. https://doi.org/10.1063/5.0014475.
(37) Darden, T.; York, D.; Pedersen, L. Particle Mesh Ewald: An N·log(N) Method for Ewald Sums in Large Systems. *J Chem Phys* **1993**. https://doi.org/10.1063/1.464397.
(38) Volkhardt, A.; Grubmüller, H. Estimating Ruggedness of Free-Energy Landscapes of Small Globular Proteins from Principal Component Analysis of Molecular Dynamics Trajectories. *Phys Rev E* **2022**, *105* (4). https://doi.org/10.1103/PhysRevE.105.044404.
(39) David, C. C.; Jacobs, D. J. Principal Component Analysis: A Method for Determining the Essential Dynamics of Proteins. *Methods in Molecular Biology* **2014**, *1084*, 193–226. https://doi.org/10.1007/978-1-62703-658-0_11.

(40) Lange, O. F.; Grubmüller, H. Can Principal Components Yield a Dimension Reduced Description of Protein Dynamics on Long Time Scales? *Journal of Physical Chemistry B* **2006**, *110* (45), 22842–22852. https://doi.org/10.1021/jp062548j.

(41) Abraham, M. J.; Murtola, T.; Schulz, R.; Páll, S.; Smith, J. C.; Hess, B.; Lindahl, E. GROMACS: High Performance Molecular Simulations through Multi-Level Parallelism from Laptops to Supercomputers. *SoftwareX* **2015**, *1–2*, 19–25. https://doi.org/10.1016/j.softx.2015.06.001.

(42) Kelich, P.; Zhao, H.; Vuković, L.; Contributed, H. Z. BinderSpace: A Package for Sequence Space Analyses for Datasets of Affinity-Selected Oligonucleotides and Peptide-Based Molecules. https://doi.org/10.1101/2023.02.15.528758.

(43) Seritan, S.; Bannwarth, C.; Fales, B. S.; Hohenstein, E. G.; Isborn, C. M.; Kokkila-Schumacher, S. I. L.; Li, X.; Liu, F.; Luehr, N.; Snyder, J. W.; Song, C.; Titov, A. V.; Ufimtsev, I. S.; Wang, L.; Martínez, T. J. TeraChem: A Graphical Processing Unit Accelerated Electronic Structure Package for Large-scale Ab Initio Molecular Dynamics. *WIREs Computational Molecular Science* **2021**, *11* (2). https://doi.org/10.1002/wcms.1494.

(44) Beyene, A. G.; Alizadehmojarad, A. A.; Dorlhiac, G.; Goh, N.; Streets, A. M.; Král, P.; Vuković, L.; Landry, M. P. Ultralarge Modulation of Fluorescence by Neuromodulators in Carbon Nanotubes Functionalized with Self-Assembled Oligonucleotide Rings. *Nano Lett* **2018**, *18* (11), 6995–7003. https://doi.org/10.1021/acs.nanolett.8b02937.

(45) Frisch, M. J.; Trucks, G. W.; Schlegel, H. B.; Scuseria, G. E.; Robb, M. A.; Cheeseman, J. R.; Scalmani, G.; Barone, V.; Mennucci, B.; Petersson, G. A.; Nakatsuji, H.; Caricato, M.; Li, X.; Hratchian, H. P.; Izmaylov, A. F.; Bloino, J.; Zheng, G.; Sonnenberg, J. L.; Hada, M.; Ehara, M.; Toyota, K.; Fukuda, R.; Hasegawa, J.; Ishida, M.; Nakajima, T.; Honda, Y.; Kitao, O.; Nakai, H.; Vreven, T.; Montgomery Jr., J. A.; Peralta, J. E.; Ogliaro, F.; Bearpark, M.; Heyd, J. J.; Brothers, E.; Kudin, K. N.; Staroverov, V. N.; Kobayashi, R.; Normand, J.; Raghavachari, K.; Rendell, A.; Burant, J. C.; Iyengar, S. S.; Tomasi, J.; Cossi, M.; Rega, N.; Millam, J. M.; Klene, M.; Knox, J. E.; Cross, J. B.; Bakken, V.; Adamo, C.; Jaramillo, J.; Gomperts, R.; Stratmann, R. E.; Yazyev, O.; Austin, A. J.; Cammi, R.; Pomelli, C.; Ochterski, J. W.; Martin, R. L.; Morokuma, K.; Zakrzewski, V. G.; Voth, G. A.; Salvador, P.; Dannenberg, J. J.; Dapprich, S.; Daniels, A. D.; Farkas, Ö.; Foresman, J. B.; Ortiz, J. V; Cioslowski, J.; Fox, D. J. Gaussian~09 Revision E.01.

(46) Zhao, Y.; Schultz, N. E.; Truhlar, D. G. Design of Density Functionals by Combining the Method of Constraint Satisfaction with Parametrization for Thermochemistry, Thermochemical Kinetics, and Noncovalent Interactions. *J Chem Theory Comput* **2006**, *2* (2), 364–382. https://doi.org/10.1021/ct0502763.

(47) Binkley, J. S.; Pople, J. A.; Hehre, W. J. *Binkley, Pople, Hehre / Small Split-Valence Basis Sets for First-Row Elements Self-Consistent Molecular Orbital Methods. 21. Small Split-Valence Basis Sets for First-Row Elements*. https://pubs.acs.org/sharingguidelines.

(48) Gordon, M. S.; Stephen Binkley, J.; John Pople, lb A.; William Pietro, lb J.; Hehre, W. J.; Binkley, J. S.; Pople, J. A.; Hehre, W. J. *Self-Consistent Molecular-Orbital Methods. 22. Small Split-Valence Basis Sets for Second-Row Elements*; 1982; Vol. 104. https://pubs.acs.org/sharingguidelines.

(49) Abd El-Mageed, A. I. A.; Handayani, M.; Chen, Z.; Inose, T.; Ogawa, T. Assignment of the Absolute-Handedness Chirality of Single-Walled Carbon Nanotubes Using Organic Molecule Supramolecular Structures. *Chemistry – A European Journal* **2019**, *25* (8), 1839–1839. https://doi.org/10.1002/chem.201900127.

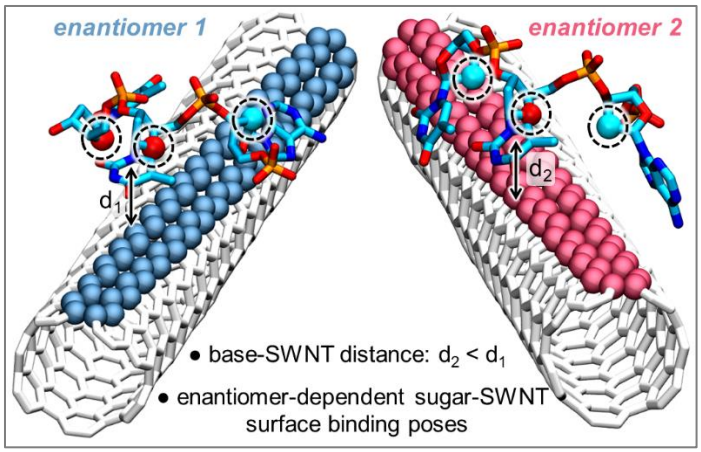

For Table of Contents Only.